



CHORUS

This is the accepted manuscript made available via CHORUS. The article has been published as:

Hydrodynamic and Ballistic Transport over Large Length Scales in

$$\frac{\text{GaAs}}{\text{AlGaAs}}$$

Adbhut Gupta, J. J. Heremans, Gitansh Kataria, Mani Chandra, S. Fallahi, G. C. Gardner, and M. J. Manfra

Phys. Rev. Lett. **126**, 076803 — Published 18 February 2021

DOI: [10.1103/PhysRevLett.126.076803](https://doi.org/10.1103/PhysRevLett.126.076803)

Hydrodynamic and ballistic transport over large length scales in GaAs/AlGaAs

Adbhut Gupta,¹ J. J. Heremans,^{1,*} Gitansh Kataria,² Mani Chandra,^{2,†} S. Fallahi,^{3,4} G. C. Gardner,^{4,5} and M. J. Manfra^{3,4,5,6,7}

¹*Department of Physics, Virginia Tech, Blacksburg, VA 24061, USA*

²*Research Division, Quazar Technologies, Sarvapriya Vihar, New Delhi 110016, India*

³*Department of Physics and Astronomy, Purdue University, West Lafayette, IN 47907, USA*

⁴*Birck Nanotechnology Center, Purdue University, West Lafayette, IN 47907, USA*

⁵*Microsoft Quantum Purdue, Purdue University, West Lafayette, IN 47907, USA*

⁶*School of Electrical and Computer Engineering,
Purdue University, West Lafayette, IN 47907, USA*

⁷*School of Materials Engineering, Purdue University, West Lafayette, IN 47907, USA*

We study hydrodynamic and ballistic transport regimes through nonlocal resistance measurements and high-resolution kinetic simulations in a mesoscopic structure on a high-mobility two-dimensional electron system in a GaAs/AlGaAs heterostructure. We evince the existence of collective transport phenomena in both regimes and demonstrate that negative nonlocal resistances and current vortices are not exclusive to only the hydrodynamic regime. The combined experiments and simulations highlight the importance of device design, measurement schemes and one-to-one modeling of experimental devices to demarcate various transport regimes.

Electron transport in metals is often governed by momentum dissipation from electrons to the lattice e.g. via impurity or phonon scattering. Such diffusive transport occurs when the momentum-relaxing (MR) electron mean-free-path ℓ_{mr} (obtained from electron mobility) is the shortest length scale in the system. However, in ultraclean two-dimensional electron systems (2DESs), a departure from diffusive transport occurs due to a long ℓ_{mr} , giving rise to either ballistic or hydrodynamic transport [1]. In the ballistic regime scattering mainly arises at the device boundaries, specularly or diffusively, and is delineated by the device scale W [2, 3]. Yet inelastic electron-electron (e-e) interactions transfer momentum predominantly among the electrons instead of to the lattice, conserving momentum within the electron system. When such momentum-conserving (MC) scattering - characterized by MC scattering mean-free-path ℓ_{mc} - dominates, electrons can move collectively like a fluid and exhibit several effects associated with fluid dynamics [1, 4–13]. The observation of this hydrodynamic regime in electronic systems has attracted significant interest [14–29].

The hydrodynamic regime shows a nonlocal current-voltage relation in devices, which can result in a negative nonlocal resistance (R_{nl}) [6–10]. Such sign reversal has been exploited in recent experiments to detect the onset of the hydrodynamic regime [19–23]. However, the ballistic regime *also* shows a nonlocal current-voltage relation, and can likewise produce negative R_{nl} [10, 11]. In fact, the ballistic regime also supports striking current vortices and collective motion of particles usually associated with fluid depictions [30]. In this work, we reveal notable current vortices in both hydrodynamic and ballistic regimes,

uniquely supported by evidence from elaborate measurements of R_{nl} . The presence of vortices in both hydrodynamic and ballistic regimes can be traced to electron momentum conservation in both regimes [10, 30].

We present strides in experimental device design, measurement schemes, and concomitant results, as well as in one-to-one modeling of the experimental device, pivotal in demarcating the transport regimes. We demonstrate measurements of R_{nl} in a large-scale ($\sim 30 \times 24 \mu\text{m}$) ultraclean ($\ell_{\text{mr}} \simeq 65 \mu\text{m}$ at 4.2 K) device, which by its scale offers exceptional sensitivity to MC scattering, and hosts 10 point contacts (PCs) to probe voltages at various distances Δx between the current injection point and voltage probes [Figs. 1(a)-1(b)]. The measurements at various Δx are critical to check against the predictions of ballistic or hydrodynamic models. The exceptionally long ℓ_{mr} , due to optimized GaAs/AlGaAs MBE growth, favors the appearance of non-diffusive transport regimes. We interpret the experimental results using realistic high-resolution simulations of quasiparticle transport at the kinetic level, involving the actual experimental geometry in the precise contact configuration, and taking into account both MR and MC scattering. The simulations with ℓ_{mr} and ℓ_{mc} as inputs, determine that the device transitions from a predominantly ballistic regime at $T = 4.2$ K to a hydrodynamic regime at $T \approx 12 - 19$ K [Fig. 1(c)].

Mesoscopic geometries were patterned on a GaAs/AlGaAs heterostructure containing a 2DES with mobility μ exceeding $670 \text{ m}^2/(\text{Vs})$ at 4.2 K. The areal electron density is $N_S \approx 3.4 \times 10^{15} \text{ m}^{-2}$, corresponding to a Fermi energy $E_F \approx 11.2 \text{ meV}$ and $\ell_{\text{mr}} = 64.5 \mu\text{m}$ at 4.2 K (Supplemental S1 [31]). To measure R_{nl} , we fabricated an in-line mesoscopic geometry [Fig. 1(a)] containing 10 PCs ($a - j$) located in barriers which are on both sides of a multiterminal Hall mesa, with sides separated by $W \approx 24 \mu\text{m}$. Each

* heremans@vt.edu
† manic@illinois.edu

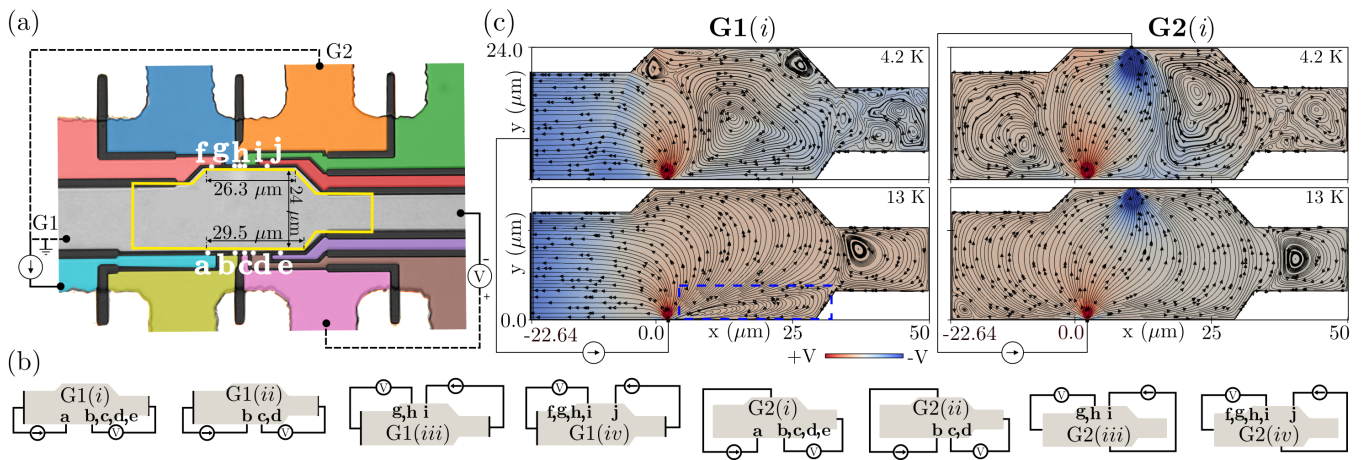


FIG. 1. (a) Optical micrograph of the geometry showing dimensions, PCs $a - j$ (indicated by white dots, with paths to PCs in distinct colors), the computational domain (yellow outline) and current and voltage PCs for example measurements in the G1(i) and G2(i) configurations. Unused PCs are left floating. (b) Schematics of subconfigurations G1($i - iv$) and G2($i - iv$) depending on current injection PC and voltage measurement PC. (c) Simulated current streamline and voltage contour plots for G1(i) and G2(i) at $T = 4.2$ K and 13 K. The streamline and source arrows depict the direction of conventional current.

PC can act as either a current injector α (injecting electrons) or a voltage detector β (detecting a nonlocal voltage). A measurement is defined by a pair consisting of an injector PC α and a detector PC β in the same barrier, and we label the center-to-center separation between PCs in such pair as $L_{\alpha\beta}$, where $L_{\alpha\beta}$ ranges from $1.3 \mu\text{m}$ to $20.5 \mu\text{m}$. Calling V_{nl} the nonlocal voltage measured at β vs a faraway counterprobe if current I is injected at α and drained at another faraway counterprobe [Fig. 1(a)], the 4-probe nonlocal resistance is expressed as $R_{\text{nl}} = V_{\text{nl}}/I$ and R_{nl} takes the sign of V_{nl} . Measurements were performed in the linear response regime i.e. for small excitation energies (such that the system is everywhere close to equilibrium, with electrons close to E_F) over $4.2 \text{ K} \leq T \leq 40 \text{ K}$, using low-frequency ($\sim 44 \text{ Hz}$) AC lock-in techniques without DC offsets. We use $I \sim 200 \text{ nA}$, which is large enough for formation of vortices (Supplemental S4 [31]) yet small enough to avoid electron heating. The conducting PC width $w \approx 0.6 \mu\text{m}$ and the Fermi wavelength, $\lambda_F = 43 \text{ nm}$ show that $w/(\lambda_F/2) \approx 28$ spin-degenerate transverse modes contribute to transport, yielding a PC resistance $\approx (h/2e^2)/28 = 461 \Omega$ (Supplemental S1 [31]). The large number of modes implies that PCs are very much open and act as classical PCs. The barriers and boundaries were defined using wet etching, which results in predominantly specular boundary scattering [36, 37]. We exploit the flexibility provided by the geometry, allowing testing of different configurations for current injector and drain, and for many Δx , in the *same* device. We use two current configurations: G1 where after injection at α , I is drained at the side of the device, and G2 where I is drained at a PC at the opposite side of the device

[Figs. 1(a)-1(b)]. The sensitivity to MC scattering turns out much higher in G1 (vicinity geometry [20]) than in G2 (Supplemental S7 [31]).

Transport in the device is modeled via the Boltzmann equation [10, 31]

$$\frac{1}{v_F} \frac{\partial f}{\partial t} + \left(\frac{\mathbf{p}}{mv_F} \right) \cdot \frac{\partial f}{\partial \mathbf{x}} = -\frac{f - f_0^{\text{mr}}}{\ell_{\text{mr}}} - \frac{f - f_0^{\text{mc}}}{\ell_{\text{mc}}}, \quad (1)$$

where $f(\mathbf{x}, \mathbf{p}, t)$ is the electron distribution in the spatial coordinates $\mathbf{x} \equiv (x, y)$, momentum coordinates $\mathbf{p} \equiv (p_x, p_y)$, and time t . While long-range electric fields are not explicitly present in Eq. (1), they are included at linear order as the gradient of the electrochemical potential [10]. The left side (with v_F the Fermi velocity and m the effective mass) describes free advection, and the right side thermalization due to MR and MC scattering in a relaxation time approximation [38] with f_0^{mr} and f_0^{mc} the local stationary and drifting Fermi-Dirac distributions (details of the model in Supplemental S2 [31] and [10]). The model inputs are ℓ_{mc} (a free parameter) and ℓ_{mr} (fixed by μ). We consider dynamics at the Fermi surface without thermal smearing so that $\mathbf{p} = mv_F \hat{p}$, and solve for transport in the zero-frequency limit ($\partial/\partial t \rightarrow 0$); v_F then factors out, leaving the circular Fermi contour as the only relevant detail. We solve Eq. (1) in the precise experimental geometry using BOLT [39], a high-resolution solver for kinetic theories. The overall prefactor of the numerical solutions is set by calibrating against the measurements in G1(ii) [Fig. 1(b)] for each T (Supplemental S3 [31]).

The experimental R_{nl} vs T for G1 and G2 are depicted in Figs. 2(a) and 2(b) respectively, for the specific $L_{\alpha\beta}$ used in measurements (Fig. 1(a) exemplifies L_{ac}).

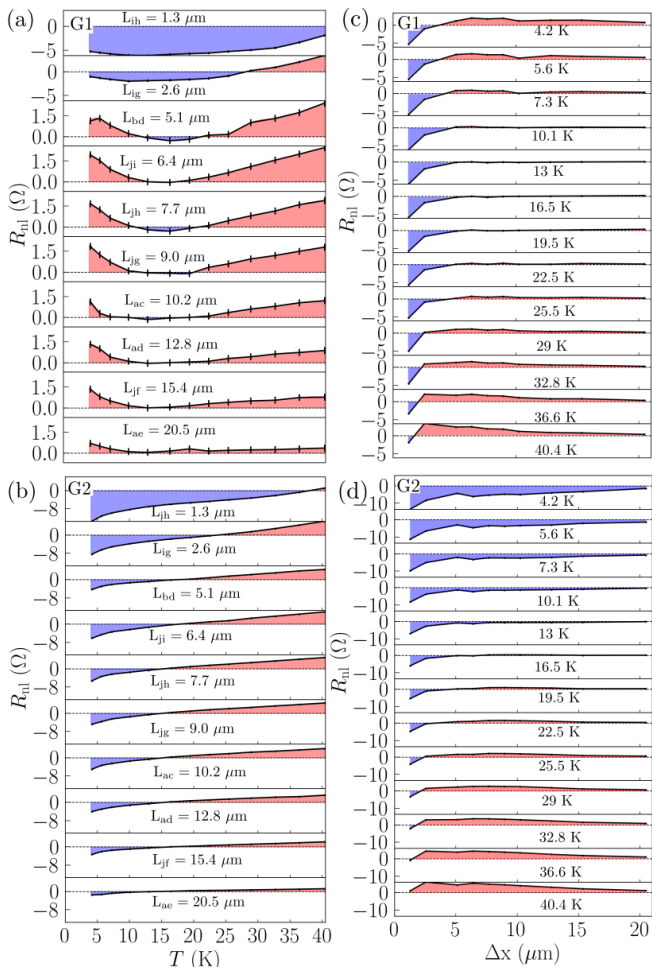


FIG. 2. (a,b) Experimental nonlocal resistance R_{nl} vs T for each $L_{\alpha\beta}$ for (a) G1 and (b) G2. (c,d) R_{nl} vs Δx for each T for (c) G1 and (d) G2. The dotted lines indicate $R_{nl} = 0$, with negative (positive) regions of R_{nl} shaded in blue (red).

Two inferences appear: the negative R_{nl} attest to a departure from diffusive transport, and a striking contrast exists in T dependences between G1 and G2. For G1, R_{nl} shows a non-monotonic dependence on T , initially decreasing as T increases, crossing over to negative values in a particular range of T for given $L_{\alpha\beta}$, then increasing to positive values. For G2, R_{nl} increases from negative values at low T to positive values at higher T . The difference in T dependence between G1 and G2 indicates that the current injector-drain configuration significantly affects transport. Figure 2(a) can be directly compared with similar results in graphene [20, 22] and other GaAs/AlGaAs experiments [19]. Figures 2(c) and 2(d) depict R_{nl} vs Δx parametrized in T for G1 and G2 respectively, tracing a crossover from negative to positive values vs Δx .

In Fig. 2(a) for $T \lesssim 10$ K, G1 shows negative R_{nl} for small $\Delta x \lesssim 2.6 \mu\text{m}$ (L_{ih}, L_{ig}), crossing over to positive R_{nl} for $\Delta x \gtrsim 5.1 \mu\text{m}$ (L_{bd}, L_{ji}, \dots). As T is in-

creased, R_{nl} vs T develops a minimum for all Δx , and the R_{nl} at this minimum crosses over to negative values for $\Delta x \lesssim 12.8 \mu\text{m}$. These observations [confirmed in Fig. 2(c)] are a consequence of the interplay between $\ell_{mc}(T)$, $\ell_{mr}(T)$ and geometry. Considering only $\ell_{mr}(T)$, with $\ell_{mr}(4.2\text{K}) = 64.5 \mu\text{m} \gg W = 24 \mu\text{m}$ at $T = 4.2$ K the system is predominantly ballistic. By finding the values of ℓ_{mc} (used as a model input parameter, given ℓ_{mr}) for which the experimental and modeled R_{nl} match, we have a means of bracketing values for $\ell_{mc}(T)$. The procedure is illustrated in Fig. 3. In Fig. 3(a) we focus on $T = 4.2$ K, lying in the region $T \lesssim 10$ K showing a crossover vs Δx from negative R_{nl} at small Δx (1.3 μm and 2.6 μm) to positive further away [see Figs. 2(a) and 2(c)]. The inset in Fig. 3(a, panel 3) shows that the limiting billiard model, common in ballistic transport and using ($\ell_{mc} \rightarrow \infty, \ell_{mr} \rightarrow \infty$), does not capture the crossover vs Δx because it results in $R_{nl} > 0$ for all Δx (inset, black trace); yet positive R_{nl} is not universal in the billiard model and can be heavily influenced by geometry (Supplemental S6 [31]). Introducing finite MR scattering via the experimental $\ell_{mr} = 64.5 \mu\text{m}$ ($T = 4.2$ K) and zero MC scattering with $\ell_{mc} \rightarrow \infty$, the modeled R_{nl} are lower compared to the billiard model but *still* do not reach $R_{nl} < 0$ at small Δx (inset, blue trace). As shown in Fig. 3(a), only with finite MC scattering using a range $\ell_{mc} \simeq 60 - 300 \mu\text{m}$ ($\gg W = 24 \mu\text{m}$), does the model yield a crossover from negative to positive R_{nl} with increasing Δx . The inset in Fig. 3(b, panel 2) plots this range at 4.2 K as compatible with data and model.

A theoretical prediction for ℓ_{mc} is found in a commonly used theoretical expression for quantum lifetime by Giuliani & Quinn (GQ) [40] (Eq. S1 in Supplemental S5 [31]), also plotted in the inset. The inset demonstrates that $\ell_{mc} \simeq 60 - 300 \mu\text{m}$ exceeds values from GQ which at 4.2 K yields $\ell_{mc} \approx 15 \mu\text{m}$. In fact, using $\ell_{mc} = 15 \mu\text{m}$ in the model yields $R_{nl} < 0$ throughout the device [Fig. 3(a), green curve], contrary to experimental observations. Recent results in fact suggest that longer ℓ_{mc} can result from dielectric screening [27]. In short, considering ℓ_{mc} , for $T \lesssim 10$ K neither the billiard model ($\ell_{mc} \rightarrow \infty$) nor GQ (too short ℓ_{mc}) reproduce the experiments, and intermediate ℓ_{mc} is required. Further, the presence of numerous current vortices of various sizes in the predominantly ballistic regime [Fig. 1(c) at 4.2 K], reveals that dominance of MC scattering is not obligatory for the formation of vortices.

For $10 \text{ K} \lesssim T \lesssim 22.5 \text{ K}$ in G1, R_{nl} vs T develops a minimum, which becomes shallower with increasing Δx , and R_{nl} crosses over to negative values for $\Delta x \lesssim 12.8 \mu\text{m}$ [Fig. 2(a)]. Modeling using $\ell_{mc} \simeq 1.5 - 5 \mu\text{m}$ accommodates all the experimental data at $T = 13$ K [Fig. 3(b)]. Since $\ell_{mc} \ll W$ and $\ell_{mc} \ll \ell_{mr}$ while $\ell_{mr} = 30.5 \mu\text{m} \gtrsim W$ is sufficiently long, the system is in the hydrodynamic regime. At $T = 13$ K, GQ yields $\ell_{mc} \simeq 2.5 \mu\text{m}$ [40], lying in the model's range of $\ell_{mc} \simeq 1.5 - 5 \mu\text{m}$. This

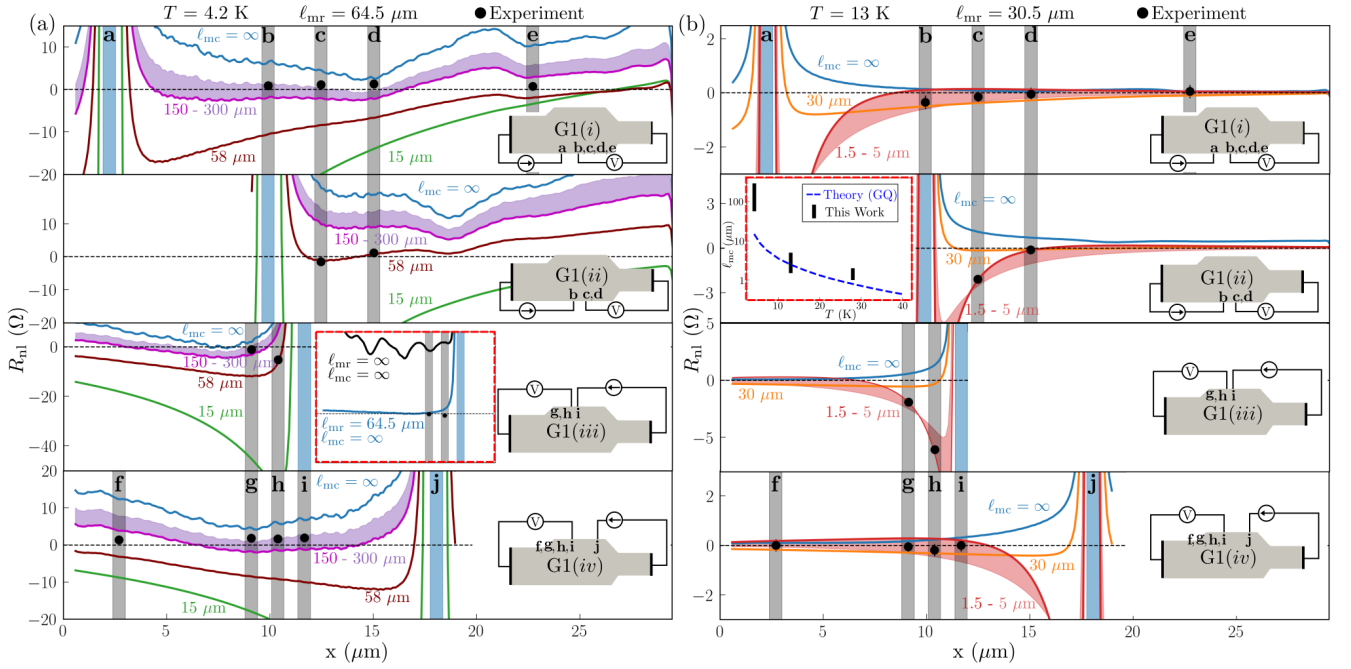


FIG. 3. Experimental R_{nl} (black dots) and modeled R_{nl} (lines) for G1($i-iv$), plotted vs location x along the barrier into which the injection PC (blue vertical bars) is placed, at (a) $T = 4.2$ K where $\ell_{mr} = 64.5 \mu\text{m}$ and (b) $T = 13$ K where $\ell_{mr} = 30.5 \mu\text{m}$. The modeled R_{nl} (lines) is shown parametrized in ℓ_{mc} . Schematics of subconfigurations are also depicted. The grey vertical bars represent locations of detector PCs. Experimental R_{nl} (black dots) for G1(ii) are chosen for reference calibration (Supplemental S3 [31]) given the clear crossover in R_{nl} in G1(ii). Inset in (a, panel 3) shows R_{nl} for G1(iii) for ($\ell_{mc} \rightarrow \infty, \ell_{mr} \rightarrow \infty$) and for ($\ell_{mc} \rightarrow \infty, \ell_{mr} = 64.5 \mu\text{m}$). Inset in (b, panel 2) shows the extracted ℓ_{mc} vs T (black bars), along with theoretical estimates (blue dotted line) from GQ [40] (Eq. S1 in Supplemental S5 [31]).

suggests that using conditions where $\ell_{mc} \gtrsim W$ (as at 4.2 K) leads to a more discriminating test of microscopic theories of ℓ_{mc} . As expected in the hydrodynamic regime, Fig. 1(c) (13 K) exhibits current vortices.

Yet the current vortices in the hydrodynamic regime in Fig. 1(c) (13 K) exhibit a distinct pattern compared to the ballistic vortices at 4.2 K. In the hydrodynamic regime only a single vortex [dashed box in Fig. 1(c)] inhabits the main chamber, and this result is obtainable from just the Navier-Stokes fluid equations. In contrast, the ballistic profile [top panels in Fig. 1(c)] shows multiple vortices, which cannot be accessed from fluid equations and require solving a Boltzmann kinetic equation. Notably, while the fluid equations cannot access the ballistic limit, the Boltzmann equation can access the fluid solutions in the limit $\ell_{mc} \ll W$.

As T is increased further in G1 to $T \gtrsim 19$ K, Fig. 2(a) shows an upward trend in R_{nl} vs T towards $R_{nl} > 0$ for all Δx . The crossover to $R_{nl} > 0$ occurs at higher T for smaller Δx (R_{nl} at $\Delta x = 1.3 \mu\text{m}$ is still negative at 40 K but is estimated to go positive around 45 K). This is corroborated by Fig. 2(c) where the region of $R_{nl} < 0$ diminishes to smaller Δx with increasing T . This behavior heralds a breakdown of hydrodynamic transport and a transition from hydrodynamic to diffusive dynamics as

MR scattering increasingly affects transport. In G1 the hydrodynamic regime exists at intermediate $T \approx 12 - 19$ K, estimated from Fig. 2(c) by tracing the crossover from negative to positive R_{nl} vs Δx . Supplemental S8 [31] shows the experimental and modeled R_{nl} at 28 K, and the change in vortex pattern with changing ℓ_{mc} .

Figures 2(b) and 2(d) reveal that in the G2 configuration $R_{nl} < 0$ occurs over a wide range of T , rendering it inefficient in differentiating between ballistic and hydrodynamic regimes. The simulations also show that G2 is *insensitive* to MC scattering (Supplemental S7 [31]). Both properties disallow using G2 to determine ℓ_{mc} , highlighting the importance of choosing appropriate contact configurations for discriminating transport regimes.

In conclusion, non-diffusive transport, either predominantly ballistic or hydrodynamic, is realized over a wide temperature range in a large-scale GaAs/AlGaAs geometry. The appearance of both predominantly ballistic or hydrodynamic regimes at such a large scale, despite opposite required limits of the strength of MC scattering, is striking. Equally remarkable are their shared characteristics of negative nonlocal resistances and current vortices. The nonlocal resistance in both regimes can be tuned by device and contact geometry, used here to disentangle the regimes and to obtain a measure of the

MC scattering length. While the importance of geometry in the ballistic regime is well-known, we additionally find that the ballistic regime can also exhibit collective effects, such as current vortices, even in the absence of dominant electron-electron interactions in a large-scale ultraclean device.

ACKNOWLEDGMENTS

The authors acknowledge support by the U.S. Department of Energy, Office of Basic Energy Sciences, Division of Materials Sciences and Engineering under awards DE-FG02-08ER46532 (JJH) and DE-SC0020138 (MJM). The authors acknowledge computational resources (GPU clusters *cascades* and *newriver*) and technical support provided by Advanced Research Computing at Virginia Tech. We thank Ravishankar Sundararaman for helpful discussions. MC thanks Sujit Kumar for hospitality during the course of this work.

-
- [1] M. J. M. de Jong, and L. W. Molenkamp, *Phys. Rev. B* **51**, 13389 (1995).
- [2] J. J. Heremans, M. B. Santos, and M. Shayegan, *Appl. Phys. Lett.* **61**, 1652 (1992).
- [3] J. J. Heremans, M. B. Santos, K. Hirakawa, and M. Shayegan, *J. Appl. Phys.* **76**, 1980 (1994).
- [4] R. N. Gurzhi, *Sov. Phys. Usp.* **11**, 255 (1968).
- [5] A. O. Govorov, and J. J. Heremans, *Phys. Rev. Lett.* **92**, 026803 (2004).
- [6] I. Torre, A. Tomadin, A. K. Geim, and M. Polini, *Phys. Rev. B* **92**, 165433 (2015).
- [7] F. M. D. Pellegrino, I. Torre, A. K. Geim, and M. Polini, *Phys. Rev. B* **94**, 155414 (2016).
- [8] L. Levitov, and G. Falkovich, *Nat. Phys.* **12**, 672 (2016).
- [9] H. Guo, E. Ilseven, G. Falkovich and, L. Levitov, *Proc. Natl. Acad. Sci. USA* **114**, 3068 (2017).
- [10] M. Chandra, G. Kataria, D. Sahdev, and R. Sundararaman, *Phys. Rev. B* **99**, 165409 (2019).
- [11] A. Shytov, J. F. Kong, G. Falkovich and, L. Levitov, *Phys. Rev. Lett.* **121**, 176805 (2018).
- [12] K. E. Nagaev, *Phys. Rev. B* **102**, 045426 (2020).
- [13] P. Ledwith, H. Guo, A. Shytov and, L. Levitov, *Phys. Rev. Lett.* **123**, 116601 (2019).
- [14] D. Taubert, G. J. Schinner, H. P. Tranitz, W. Wegscheider, C. Tomaras, S. Kehrein, and S. Ludwig, *Phys. Rev. B* **82**, 161416(R) (2010).
- [15] D. Taubert, G. J. Schinner, C. Tomaras, H. P. Tranitz, W. Wegscheider, and S. Ludwig, *J. Appl. Phys.* **109**, 102412 (2011).
- [16] P. J. W. Moll, P. Kushwaha, N. Nandi, B. Schmidt, and A. P. Mackenzie, *Science* **351**, 1061 (2016).
- [17] G. M. Gusev, A. D. Levin, E. V. Levinson, and A. K. Bakarov, *AIP Advances* **8**, 025318 (2018).
- [18] B. A. Braem, F. M. D. Pellegrino, A. Principi, M. Rösli, C. Gold, S. Hennel, J. V. Koski, M. Berl, W. Dietsche, W. Wegscheider *et al.*, *Phys. Rev. B* **98**, 241304(R) (2018).
- [19] A. D. Levin, G. M. Gusev, E. V. Levinson, Z. D. Kvon, and A. K. Bakarov, *Phys. Rev. B* **97**, 245308 (2018).
- [20] D. A. Bandurin, I. Torre, R. K. Kumar, M. B. Shalom, A. Tomadin, A. Principi, G. H. Auton, E. Khestanova, K. S. Novoselov, I. V. Grigorieva *et al.*, *Science* **351**, 1055 (2016).
- [21] R. K. Kumar, D. A. Bandurin, F. M. D. Pellegrino, Y. Cao, A. Principi, H. Guo, G. H. Auton, M. B. Shalom, L. A. Ponomarenko, G. Falkovich *et al.*, *Nat. Phys.* **13**, 1182 (2017).
- [22] D. A. Bandurin, A. V. Shytov, L. S. Levitov, R. K. Kumar, A. I. Berdyugin, M. B. Shalom, I. V. Grigorieva, A. K. Geim, and G. Falkovich, *Nat. Commun.* **9**, 4533 (2018).
- [23] A. I. Berdyugin, S. G. Xu, F. M. D. Pellegrino, R. K. Kumar, A. Principi, I. Torre, M. B. Shalom, T. Taniguchi, K. Watanabe, I. V. Grigorieva *et al.*, *Science* **364**, 162 (2019).
- [24] V. Galitski, M. Kargarian, and S. Syzranov, *Phys. Rev. Lett.* **121**, 176603 (2018).
- [25] D. Svintsov, *Phys. Rev. B* **97**, 121405(R) (2018).
- [26] J. Gooth, F. Menges, N. Kumar, V. Süß, C. Shekhar, Y. Sun, U. Drechsler, R. Zierold, C. Felser, and B. Gotsmann, *Nat. Commun.* **9**, 4093 (2018).
- [27] M. Kim, S. G. Xu, A. I. Berdyugin, A. Principi, S. Slizovskiy, N. Xin, P. Kumaravadivel, W. Kuang, M. Hamer, R. K. Kumar *et al.*, *Nat. Commun.* **11**, 2339 (2020).
- [28] M. J. H. Ku, T. X. Zhou, Q. Li, Y. J. Shin, J. K. Shi, C. Burch, L. E. Anderson, A. T. Pierce, Y. Xie, A. Hamo *et al.*, *Nature* **583**, 537 (2020).
- [29] O. E. Raichev, G. M. Gusev, A. D. Levin, and A. K. Bakarov, *Phys. Rev. B* **101**, 235314 (2020).
- [30] M. Chandra, G. Kataria, and D. Sahdev, arXiv:1910.13737 (2019).
- [31] See Supplemental Material at [...] which includes Refs. [7, 10, 32–35, 40] for 2DES properties, modeling calibration, conditions for vortices, effects of geometry and contact configuration, and effect of MR scattering at higher temperatures.
- [32] G. C. Gardner, S. Fallahi, J. D. Watson, and M. J. Manfra, *J. Cryst. Growth* **441**, 71 (2016).
- [33] W. Zawadzki, and W. Szymańska, *Phys. Status Solidi B* **45**, 415 (1971).
- [34] W. Zawadzki, *J. Phys.: Condens. Matter* **29**, 373004 (2017).
- [35] J. J. Harris, C. T. Foxon, D. Hilton, J. Hewett, C. Roberts, and S. Auzoux, *Surf. Sci.* **229**, 113 (1990).
- [36] J. J. Heremans, S. von Molnár, D. D. Awschalom, and A. C. Gossard, *Appl. Phys. Lett.* **74**, 1281 (1999).
- [37] H. Chen, J. J. Heremans, J. A. Peters, A. O. Govorov, N. Goel, S. J. Chung, and M. B. Santos, *Appl. Phys. Lett.* **86**, 032113 (2005).
- [38] We restrict ourselves to solutions of the Boltzmann equation in which MC scattering is parametrized with a single relaxation timescale. Ref. [12, 13] report on transport phenomena that can result from a more sophisticated collision integral.
- [39] M. Chandra, S. Sankaran, and P. Yalamanchili, github.com/mchandra/bolt.
- [40] G. F. Giuliani, and J. J. Quinn, *Phys. Rev. B* **26**, 4421 (1982).